GEOPHYSICS, VOL. 69, NO. 6 (NOVEMBER-DECEMBER 2004); P. 1478–1490, 21 FIGS.
10.1190/1.1836821

Diffraction imaging by focusing-defocusing: An outlook on seismic superresolution

V. Khaidukov[1], E. Landa[2], and T. J. Moser[3]

ABSTRACT

Diffractions always need more advertising. It is true that conventional seismic processing and migration are usually successful in using specular reflections to estimate subsurface velocities and reconstruct the geometry and strength of continuous and pronounced reflectors. However, correct identification of geological discontinuities, such as faults, pinch-outs, and small-size scattering objects, is one of the main objectives of seismic interpretation. The seismic response from these structural elements is encoded in diffractions, and diffractions are essentially lost during the conventional processing/migration sequence. Hence, we advocate a diffraction-based, data-oriented approach to enhance image resolution—as opposed to the traditional image-oriented techniques, which operate on the image after processing and migration. Even more: it can be shown that, at least in principle, processing of diffractions can lead to superresolution and the recovery of details smaller than the seismic wavelength.

The so-called reflection stack is capable of effectively separating diffracted and reflected energy on a prestack shot gather by focusing the reflection to a point while the diffraction remains unfocused over a large area. Muting the reflection focus and defocusing the residual wavefield result in a shot gather that contains mostly diffractions. Diffraction imaging applies the classical (isotropic) diffraction stack to these diffraction shot gathers. This focusing-muting-defocusing approach can successfully image faults, small-size scattering objects, and diffracting edges. It can be implemented both in model-independent and model-dependent contexts. The resulting diffraction images can greatly assist the interpreter when used as a standard supplement to full-wave images.

INTRODUCTION

Diffractions are the abandoned stepchildren of traditional seismic processing and imaging. Routine practice uses specular reflections to estimate the subsurface velocity distribution and reconstruct the geometry of strong and smooth reflectors—most often with success. At the same time, however, correct identification of geological discontinuities, such as faults, pinch-outs, and small-size scattering objects, is an important problem in interpretation of seismic data. Local structural and lithological elements in the subsurface of a size comparable to the wavelength are usually ignored during processing and identified only during interpretation. Unfortunately, the reliability of such identification is generally low. It is precisely the seismic response from these structural elements that is encoded in the diffracted wavefield.

The importance of diffracted/scattered waves has long been recognized (Krey, 1952; Hagedoorn, 1954). Landa et al. (1987) and Kanasewich and Phadke (1988) proposed to construct a common-diffraction section by stacking the signal along a diffraction hyperbola instead of the conventional common-mid point (CMP) hyperbola. Papziner and Nick (1998) extracted diffraction energy from ground-penetrating radar (GPR) data to detect small objects in georadargrams. Landa and Keydar (1998) used shallow diffractions to survey the digging of a tunnel. Goldin et al. (2000) proposed a Gaussian beam decomposition for detection of diffraction objects. In his provoking sequence of papers, Neidell (1997) distinguished between reflective and diffractive contributions to the wavefield, and recognized the diffractive component as a key ingredient in establishing resolution—or even superresolution (the recovery of details smaller than the seismic wavelength). An illustration

Published on Geophysics Online June 7, 2004. Manuscript received by the Editor September 22, 2003; revised manuscript received January 26, 2004.
[1]Siberian Branch of Russian Academy of Science, Geophysical Institute, pr.Koptyuga 3, Novosibirsk, Russia. E-mail: kvg@uiggm.nsc.ru.
[2]OPERA (Applied Geophysical Research Group), Pau University, Batiment I.F.R. rue Jules Ferry, 64000 Pau, France; on leave from Geophysical Institute of Israel, Lod, Israel. E-mail: evgeny.landa@univ-pau.fr.
[3]Fugro-Jason BV, c/o van Alkemadelaan 550A, 2597 AV The Hague, The Netherlands. E-mail: tmoser@fugro-jason.com; mosertj@hotmail.com.

of resolution improvement by means of the diffractive component in vertical seismic profile (VSP) data imaging can be found in Moser et al. (2000). An early report (Zavalishin, 1982) suggested an interesting, but until now untested, application of diffractions in 4D/time-lapse reservoir studies. Imaging of small scattering objects by means of diffractions has obvious applications in environmental and archeological studies.

In this paper, we promote diffraction imaging as a supplement to the conventional reflection imaging to be used in mainstream processing and imaging. We propose an imaging algorithm that is intentionally diffraction biased, instead of reflection biased. The crucial point here is to find a domain where the diffracted and reflected waves are well separated from each other [see Nemeth et al. (2000), where an extensive review on signal separation methods is given]. Our approach is based on focusing reflected waves to their imaginary source points and then muting them from the full wavefield. Reflection focusing can be achieved by the so-called reflection-stack type of migration. This suggestion was raised by Timoshin (1978), but received only little attention since then (Zavalishin, 2000). Because of different moveout properties (or integration curves), diffraction and reflection focusing are fundamentally different. Whereas the first is a standard tool in migration to stack energy along elementary diffractions at their respective elementary sources, together making up a reflecting surface, the second stacks energy along real reflection events and transports it to mirrored points on the opposite side of the reflector. Therefore, the reflection-stacked energy is typically concentrated twice as deep as the diffraction-stacked energy, and we have, in principle, obtained a separation. Based on this idea, the outline of our algorithm is (1) apply the reflection stack to the full-wave shot gather, (2) mute areas with strongly focused energy, (3) reconstruct the shot gather, now with mostly diffracted energy, and (4) apply the diffraction stack to this diffracted shot gather.

We develop this algorithm in detail for the macromodel independent case, and indicate briefly how it can be implemented when an accurate velocity model is available. The potential of the proposed diffraction imaging is demonstrated on two synthetic models, and on the Pluto data set (which is also synthetic, but of considerable complexity, simulating a Gulf of Mexico deep-water subsalt prospect). We start with a review of geometrical aspects of diffractions and elaborate on their relation to seismic superresolution.

DEFINITIONS AND GEOMETRICAL ASPECTS

The general validity conditions of ray theory (Červený, 2001) are a useful and commonly accepted framework to define diffractions and reflections, and to distinguish between them. Seismic waves can be modeled by ray theory in the high-frequency limit or, equivalently, if the wavelength is much smaller than any characteristic length scale in the propagation medium. In particular, Snell's law and specular reflection adequately describe backscattering from a discontinuous boundary in the medium provided that the wavelength is small compared to the radius of curvature of the boundary. Therefore, we define a reflection as the seismic response from a sufficiently smooth interface. On the other hand, if the curvature of the interface increases and its radius becomes of the order of the wavelength itself, ray theory is no longer valid. We define the seismic response from a strongly curved interface that does not satisfy the ray validity conditions as a diffraction. With such a definition, we examine two important special cases. First, if the interface curvature locally grows to infinity, an edge or tip appears, and the diffractions on it are edge or tip waves (Klem-Musatov, 1994). Second, if the size of an isolated scattering object of arbitrary shape shrinks to zero, the backscattered waves from it are diffractions. The dynamical behavior of these types of waves is different, but we consider only kinematical aspects of diffractions in this paper, so they do not need to be distinguished. In any case, it is important to stress that the ray-theory criteria are only qualitative, and that there is no sharp distinction between reflections and diffractions. Rather, they are extreme cases of the same backscattering phenomenon, depending on frequency and characteristic lengths of the discontinuity. We call *diffraction imaging* the classical diffraction stack, but applied to shot gathers in which reflections have been (ideally) removed, or at least attenuated.

Let us recall some basic geometrical properties relevant for the reflection focusing presented below (Keller, 1962; Trorey, 1970; Berryhill, 1977; de Bazelaire, 1988). As a rule of thumb, reflections and diffractions from a discontinuity at the same depth differ in moveout and the position of the traveltime apex in the shot gathers. This can be understood by considering reflections as originating from an imaginary source that is mirrored with respect to its reflector. In the simplest case of a plane horizontal topography, a plane horizontal reflector, and a constant velocity in between, the reflection traveltime curve is a hyperbola with its apex at zero offset. If the source moves to a next location, its mirror point and the reflection hyperbola move along with it unchanged, so that all reflection shot gathers are identical. On the other hand, the traveltime curve of a point diffractor is a hyperbola with its apex fixed above the diffractor. If the source moves to a next location, the diffraction hyperbola does not move laterally, but only vertically. Hence, diffractions can appear anywhere on the shot gathers. The moveout is controlled by the position of the asymptotes of the hyperbola. The slopes of the asymptotes are the same for a given medium, but for the plane horizontal reflector they start at time zero, while for the point diffractor they start at a nonzero time, equal to the propagation time from source to diffractor. Diffraction curves have steeper dips and exist over a more narrow range of offsets in a shot gather than reflection curves. These properties apply strictly only for a horizontal reflector model and a point diffractor at the same depth. However, for more general geometries, where moveout can be nonhyperbolic, they are still qualitatively valid and useful. Again, depending on frequency content, there is no sharp distinction between reflections and diffractions, and their properties. Figure 1 illustrates the geometrical properties for the simple cases of the plane horizontal reflector and point diffractor, but also for such intermediate cases as a dipping and curved reflector. The differences in moveout have a direct impact on the focusing properties discussed below. The property that, contrary to reflections, diffraction apices are laterally invariant with respect to source location can be exploited in a multisource data acquisition: if the diffraction is too close to a reflection to be isolated in one shot gather, then there is a likely greater separation in another one. For many shots, we can even benefit from a statistical reduction of the reflective component. This is important for edge diffractions, which are

often locally tangent to reflections from the same discontinuity (Klem-Musatov, 1994).

DIFFRACTIONS AND SUPERRESOLUTION

The main goal of diffraction imaging is to increase image resolution, delineate faults and edges, and facilitate interpretation. Several approaches exist aimed at enhancing the resolution on poststack and postmigration seismic images. Removal of the wavelet effect by deconvolution is a common practice, which often reveals structural details masked in the (band-limited) seismic image. Gersztenkorn and Marfurt (1999) extract coherence measures from a neighborhood of an image point. Hu et al. (2001) propose a deblurring filter, Fehmers and Höckers (2003) a structure-oriented filter. Such techniques indeed improve the interpretability of the seismic image.

We take a more conservative viewpoint here. The Rayleigh criterion poses a limit on the resolution to be extracted from a recorded backscattered wave (Born and Wolf, 1959; Chen and Schuster, 1999). If no a priori information is available in the scatterer geometry, no details smaller than half the wavelength are recoverable. This limit is imposed by the band-limited nature of the far-field scattered wave and the general impossibility to extrapolate outside its frequency band. Wave propagation acts as a low-pass filter. Hence, deconvolution-type techniques may transform the seismic image into an image that has more detail and, indeed, may be easier to interpret. However, the reliability of these details is to be considered low, and uncertainty measures are not available. Below the Rayleigh limit, no definite answers can be given as to location, dip, and curvature of a discontinuity, nor even to topological properties, such as connectivity. Instead, there is room for more or less arbitrary interpretation, not related to or justified by the physics of the wave propagation. Even worse, migration artifacts, due to under- or overmigration, are a common problem in seismic images. The artifacts usually manifest themselves as apparent edges (Figure 2). Without further information, it is impossible to identify migration artifacts, and they will be mistaken for structural details (especially by the automated methods mentioned above). In other words, an image-driven approach to resolution enhancement is inherently limited.

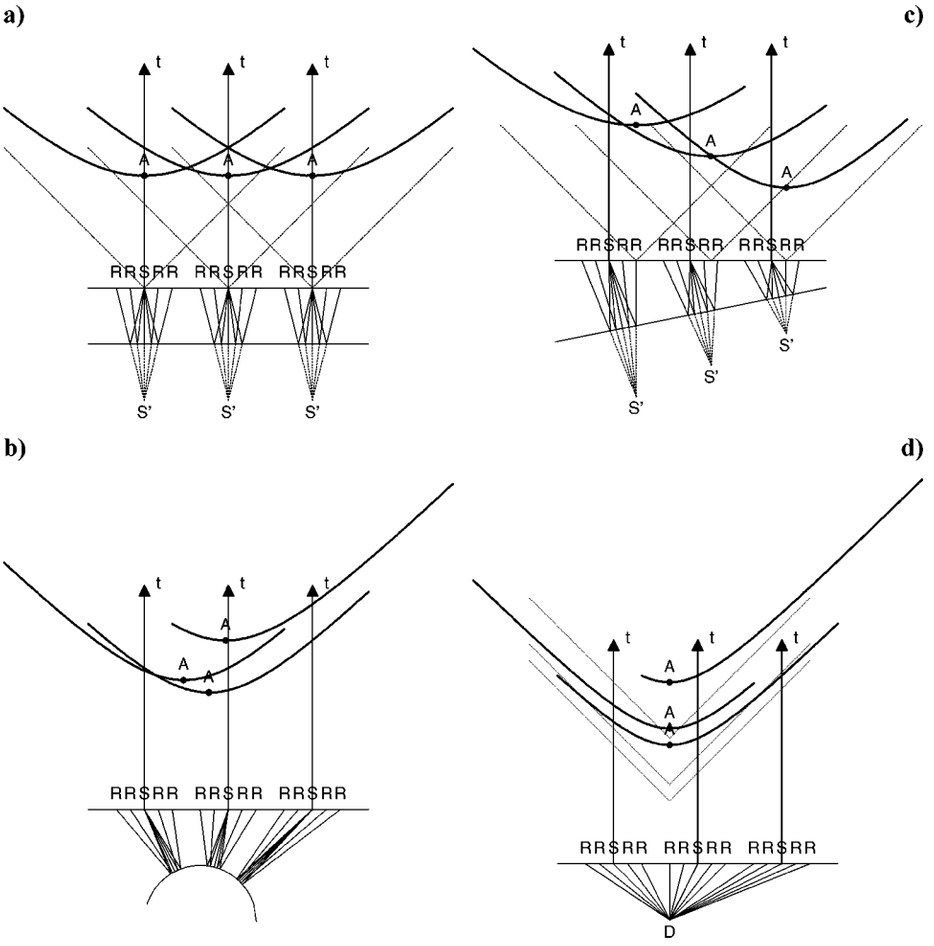

Figure 1. Geometry of reflection and diffraction. S, R denote source and receiver locations, respectively; S' the imaginary reflection source; A the reflection/diffraction hyperbola apex; and *t* the traveltime. (a) Reflections on a horizontal plane reflector. (b) Reflections on a strongly curved reflector. (c) Reflections on a dipping reflector. (d) Diffractions on a point diffractor (denoted by D).

Superresolution, the recovery of subwavelength scale details in a seismic image, is however achievable under certain idealized circumstances. Full-band information of the scatterer can be recovered from the far-field scattered wavefield if out-of-band extrapolation is possible, which, in turn, is possible if the size of the scatterer itself is of the order of the wavelength (Bertero et al., 1997). Several algorithms are available to perform this out-of-band extrapolation (Gerchberg, 1974). These algorithms may be difficult to implement in many practical cases of seismic imaging. The important implication is, however, that if the full wavefield is decomposed in reflection and diffraction components, the diffractive components can be identified as carriers of superresolution information coming from scatterers of subwavelength scale. Isolating diffractions from the full wavefield and imaging them separately is therefore a first step in establishing superresolution of structural details—and this is the objective of this paper.

As for the case of full-wave imaging, the reliability of diffraction imaging depends on the accuracy of the migration velocity, and uncertainties can be assessed by checking the flatness of common-image gathers (just as for full-wave images, diffraction images should be consistent for all offsets). Moreover, diffraction images do not suffer from apparent edges caused by migration artifacts; the artifacts in Figure 2 are not caused by diffractive energy, but by caustics due to traveltime triplication, so a diffraction analysis will help to unmask them. Thanks to these properties, diffraction imaging stands out in contrast to the image-driven approach discussed above, as an objective tool for high (or super-) resolution image analysis and, above all, justified by the physics of wave propagation. As such, diffraction images are to be seen as a complement to reflection images and should be made available for the interpreter as an aid to reliable high-resolution interpretation.

Separating diffractions from the full wavefield requires an unconventional approach to seismic processing. Many steps in traditional time processing [such as velocity analysis, normal moveout (NMO), stack] are, implicitly or explicitly, designed to detect and image specular reflection events without honoring the special geometry of (real) diffractions. For instance, NMO and stack to zero offset suppress energy aligned along diffraction hyperbolas with apices at nonzero offsets. Also, dip moveout (DMO) explicitely deals with dipping reflectors, whereas diffractors have no well-defined dip. For these reasons, in order to benefit as much as possible from diffractions and the information they convey, we analyze them in the prestack domain and before migration. Diffraction imaging is, therefore, essentially a data-driven approach to image resolution.

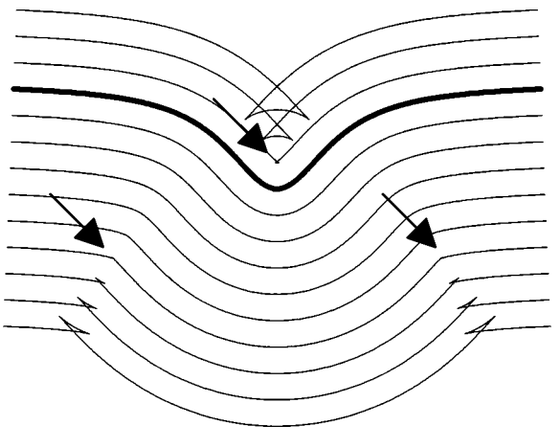

Figure 2. Over- and undermigration of a simple syncline, due to velocity errors. For a too low overburden migration velocity, the image shifts upward; for a too high velocity, it shifts downward, occupying equidistant curves to the syncline. Migration artifacts, indicated by arrows, appear as diffraction edges.

In the following section, we present an approach to attenuate reflections and enhance the diffractive component. While we acknowledge that the choice of an imaging principle is relevant for resolution (Levin, 1998), we leave this out of the discussion in this paper. In many implementations, the migration integral kernel is derived assuming locally plane reflectors (Beylkin, 1985), or using a high-frequency or stationary-phase approximation (Docherty, 1991), and therefore biased towards specular reflections. Emphasizing reflectivity also has implications for illumination of, for example, steep reflectors, which we will not discuss here. We use the classical diffraction stack, with an unbiased, isotropic integral kernel. In fact, as we argue below, *even* the classical diffraction stack is biased towards reflections.

REFLECTION FOCUSING AND DIFFRACTION IMAGING

A key observation is that the classical diffraction stack deals with reflections and diffractions in a fundamentally different way. We consider the diffraction stack V for a subsurface location $\mathbf{x}$ in the form (Tygel et al., 1996)

$$V(\mathbf{x}) \sim \int \mathrm{d}\boldsymbol{\xi} \int \mathrm{d}t\, U(\boldsymbol{\xi}, t)\delta(t - t_d(\boldsymbol{\xi}, \mathbf{x})), \qquad (1)$$

where $U(\boldsymbol{\xi}, t)$ represents the recorded seismic data, for an arbitrary source-receiver configuration parametrized by the generic vector $\boldsymbol{\xi}$ (Hubral et al., 1996), and $t_d(\boldsymbol{\xi}, \mathbf{x})$ is the diffraction traveltime curve ($\boldsymbol{\xi}$ is integrated over the measurement aperture, and the time t over the relevant time interval). The stack 1 incorporates an isotropic weighting factor, affecting the amplitude only, which we do not specify here. The diffraction traveltime $t_d(\boldsymbol{\xi}, \mathbf{x})$ is the propagation time from source to receiver via a hypothetical diffraction point $\mathbf{x}$.

For reflections from continuous interfaces, the physical principle justifying the diffraction stack (equation 1) is that (1) a reflector can be composed of an infinitely dense set of point diffractors, (2) its reflective response is the superposition of elementary diffractions from these points, and (3) the reflection traveltime curve is the envelope of the elementary diffraction traveltime curves. In this case, the elementary diffractions are merely mathematical idealizations, destined to interfere constructively along reflectors, and destructively elsewhere, due to Huygens' principle. They are abstractions and cannot be observed independently. When the recorded data $U(\boldsymbol{\xi}, t)$ include the full reflected wavefield, the envelopes of the elementary diffraction curves lie tangent to the reflection curves, and the reflections are imaged tangent to their corresponding reflectors.

For real diffractions originating from truncated reflectors, edges, or small-scale scattering objects, the situation is completely different: (1) real diffractors are not the infinitesimal components of a larger smooth interface, but rather stand alone; (2) their diffractive response does not contribute constructively to a larger seismic event, it is not an abstraction

and is really observable; and (3) their traveltime curves do not contribute to an envelope curve. Their amplitude, however, is considerably smaller than that of reflections, so they are likely to be hidden in the diffraction stack (equation 1). To prevent the diffractive component from being lost, it is necessary to separate it from the full wavefield and image it separately. This is the essence of diffraction imaging.

In order to accomplish the separation, we propose to focus the reflections to their own imaginary sources (as defined in the section "Definitions and geometrical aspects"). First, we give an outline of the general idea, and in the following section we discuss the implementation. The reflection focusing is illustrated in the simple case of Figure 3 (Timoshin, 1978; Zavalishin, 2000). The classical diffraction stack 1 maps reflections (Figure 3, left) to curves whose envelopes constitute the reflector, and diffractions (Figure 3, right) to single points that are usually too weak to be distinguished. By replacing the diffraction traveltime curve by a reflection time curve $t_r(\boldsymbol{\xi}, \mathbf{x})$, the stack 1 becomes a reflection focusing operator,

$$V^R(\mathbf{x}) \sim \int \mathrm{d}\boldsymbol{\xi} \int \mathrm{d}t\, U(\boldsymbol{\xi}, t)\delta(t - t_r(\boldsymbol{\xi}, \mathbf{x})), \qquad (2)$$

which focuses the reflection to the much deeper point z_{im}, while the diffraction remains unfocused. Here, the different moveouts of the reflection and diffraction hyperbolas play an essential role, as discussed above under geometrical aspects. We refer to $V^R(\mathbf{x})$ as the *reflection focus image*. Since the reflection imaginary sources are much deeper than the corresponding reflectors, the depth range of $V^R(\mathbf{x})$ is typically twice that of the classical diffraction stack $V(\mathbf{x})$.

If the reflection traveltimes $t_r(\boldsymbol{\xi}, \mathbf{x})$ are calculated correctly, application of the reflection stack (equation 2) to a common-shot gather will focus the reflected energy from a continuous smooth interface to its imaginary source point. On the other hand, diffracted energy from edges or small-scattering objects at the same depth will be unfocused over large areas. Thus, in contrast to the diffraction stack 1, the reflection stack (equation 2) is a transformation of the shot gather to a domain where reflections and diffractions can be separated. In this reflection focus domain, we mute $V^R(\mathbf{x})$ in areas with strongly focused energy and denote it $V_0^R(\mathbf{x})$. To $V_0^R(\mathbf{x})$, which only contains the residual diffracted energy, we apply the defocusing operator

$$U^D(\boldsymbol{\xi}, t) \sim \int \mathrm{d}\mathbf{x}\, V_0^R(\mathbf{x})\delta(t - t_r(\boldsymbol{\xi}, \mathbf{x})). \qquad (3)$$

Here, $t_r(\boldsymbol{\xi}, \mathbf{x})$ is again the reflection traveltime, and the integration of $\mathbf{x}$ is over the whole image. The right-hand side of equation 3 is a Kirchhoff-type demigration integral (Santos et al., 2000). For the same set of traveltime curves, the focusing and defocusing integral are dual to each other—we stress this by keeping the δ-factors in equations 1–4.

Depending on the quality of the reflection focus and the amount of muting, the new data set $U^D(\boldsymbol{\xi}, t)$ contains mainly diffractions. The final step, which is the actual diffraction imaging, is then more or less trivial and consists of applying the original diffraction stack (equation 1) to the diffracted wavefield $U^D(\boldsymbol{\xi}, t)$:

$$V^D(\mathbf{x}) \sim \int \mathrm{d}\boldsymbol{\xi} \int \mathrm{d}t\, U^D(\boldsymbol{\xi}, t)\delta(t - t_d(\boldsymbol{\xi}, \mathbf{x})). \qquad (4)$$

Unlike the integral in expression 1, the integral in expression 4 involves a superposition of only real existing diffractions and not of elementary diffractions. Also, it is essential to note that the integral in expression 4 is indeed the classical isotropic diffraction stack, without a kernel biased towards specular reflections or high-frequency backscattering.

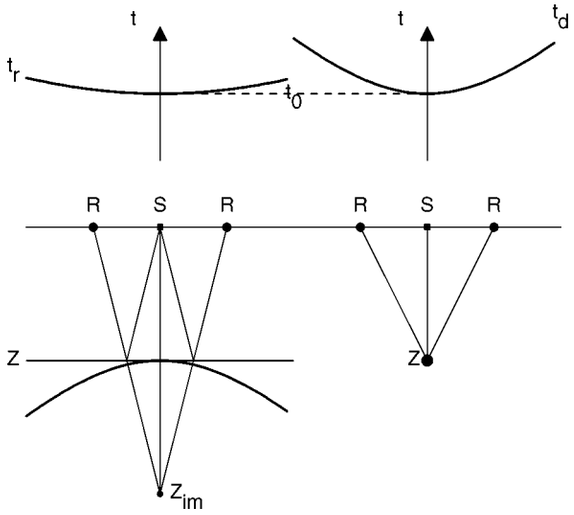

Figure 3. Reflection focusing (after Zavalishin, 2000). The wavefronts of both reflected and diffracted waves are restored by conventional migration at an instant $t = z/v$, where v is the subsurface seismic velocity. The wavefront of the extrapolated diffracted wave is focused to a point (right), whereas the wavefront of the extrapolated reflected wave is tangent to the reflector. Focusing of the reflection would occur at the instant $t = 0$ at the imaginary source point z_{im}(left).

IMPLEMENTATION

It remains to find or define a proper reflection traveltime curve $t_r(\boldsymbol{\xi}, \mathbf{x})$ that optimally focuses the reflective wavefield component. This is a nontrivial task. In situations where the velocity model is accurately known (for instance, in the framework of prestack depth migration), the reflection time can be found by ray tracing (similarly to the conventional diffraction time t_d):

$$t_r(\boldsymbol{\xi}, \mathbf{x}) = T(\mathbf{x}, \mathbf{x}_r)$$
$$t_d(\boldsymbol{\xi}, \mathbf{x}) = T(\mathbf{x}_s, \mathbf{x}) + T(\mathbf{x}, \mathbf{x}_r) \qquad (5)$$

where $\mathbf{x}_s$ and $\mathbf{x}_r$ are source and receiver locations, $\mathbf{x}$ the diffraction or reflection focusing point, and T the ray-based traveltime (possibly multivalued). If the migration velocity is adequate enough to focus elementary diffractions to elementary diffraction points, it is also capable of focusing reflections to imaginary reflection source points (which, as noted before, are located twice as deep). The sequence of applying expression 2, muting, applying expression 3, and finally applying expression 4 is then relatively easy to implement. Diffractivity analysis assuming an accurate velocity model from first break times was presented for VSP by Moser et al. (2000).

Often, the assumption of a good velocity is not justified. This does not impede reflection focusing, however. The dual character of the focusing and defocusing integrals, even for general

traveltime-curve systems or a wrong velocity, implies that an accurate velocity is not required to reconstruct the shot gather after parts of the reflection focus image have been muted. In fact, the degree of attenuation of reflected energy depends only on the quality of the focusing and the amount of muting. It is important *that* the reflection energy is focused, and not *where* it is focused. Moreover, because of the absence of a sharp distinction between diffractions and reflections, a complete removal of reflections is often not feasible. In cases of an inaccurate, wrong, or unknown velocity model, which are in fact all conceptually equivalent, the focusing has to be accomplished by means of an additional focusing parameter. In all cases, an incomplete focusing implies that the reflection energy is not reduced to a point, but rather to a sharp localized caustic, which can be dealt with, to a certain extent, by muting.

We concentrate here on the case of an unknown subsurface model and implement the reflection focusing in a macromodel independent context. We take the so-called homeomorphic imaging common shot point approximation (HICSP) (Keydar et al., 1996) as a starting point to approximate the reflection traveltime curve. Restricted to common-shot gathers, the homeomorphic imaging principle assumes that the reflected wave can be locally approximated by a spherical wave with the HICSP reflection curve. In two dimensions, it reads

$$t_r(h,\mathbf{x}) = t_0 + \left(\sqrt{R_0^2 + 4R_0 h \sin\beta_0 + 4h^2} - R_0\right)\Big/ v, \quad (6)$$

where v is the near-surface velocity (assumed constant and known), h half the source-receiver offset, t_0 the arrival time at zero offset, and R_0 and β_0 the radius and emergence angle of the spherical wave, respectively. As a function of h, equation 6 is a shifted hyperbola, with R_0 and β_0 as free parameters. We take them as polar coordinates with respect to the source point of an imaginary reflection source point $\mathbf{x} = (x_{im}, z_{im})$. The point $\mathbf{x}$ is not defined in the actual depth domain, but in an auxiliary depth model with constant velocity v and parametrized by (x_{im}, z_{im}); we refer to this as a *pseudodepth domain*. Upon substituting $R_0^2 = x_{im}^2 + z_{im}^2$ and $\sin\beta_0 = x_{im}/R_0$, the reflection curve reads

$$t_r(h,\mathbf{x}) = t_0 + \left(\sqrt{(x_{im}+2h)^2 + z_{im}^2} - \sqrt{x_{im}^2 + z_{im}^2}\right)\Big/ v. \quad (7)$$

An essential ingredient of homeomorphic imaging is to take t_0 independent of R_0 in order to allow waves of all curvatures to arrive at all times. In the most general case, a reflection focus image has to be constructed for each t_0 separately:

$$V^R(t_0; x_{im}, z_{im}) = \int \mathrm{d}h\, U(h, t_r(h,\mathbf{x})), \quad (8)$$

where $t_r(h,\mathbf{x})$ is given by equation 7. For each t_0, the optimal R_0 and β_0 are found by a grid search for the maximum of $|V^R|$ in the pseudodomain (x_{im}, z_{im})—the reflection focuses to one point, or in a localized caustic, depending on the hyperbolicity of the real reflection event. This search is equivalent to the multifocusing or common reflection surface (CRS) search for optimal R_0 and β_0 (Landa et al., 1999a), except that we keep the entire image V^R, including the nonoptimal parts, to be able to reconstruct the shot gather. Indeed, V^R is muted by zeroing strongly focused energy (located around the maximum of $|V^R|$) and taking care of a smooth transition to unmuted regions. The result is $V_0^R(t_0; x_{im}, z_{im})$. The inverse to equation 8 is the defocusing integral

$$U^D(t_0; h, t) = \int \mathrm{d}x_{im} \int \mathrm{d}z_{im}\, V_0^R(t_0; x_{im}, z_{im}) \times \delta(t - t_r(h,\mathbf{x})), \quad (9)$$

where $t_r(h,\mathbf{x})$ is again given by equation 7. For each t_0, $U^D(t_0; h, t)$ is a shot record in which the (hypothetical) reflection event passing through t_0 has been optimally attenuated; reflections with zero-offset times other than t_0 will be less than optimally attenuated. Again in the most general case, the procedure 8–9 has to be repeated for each t_0 and the final diffraction shot gather $U^D(h, t)$ has to be composed from the individual $U^D(t_0; h, t)$, each time suppressing one reflection event at a time. In practical cases, however, this can be restricted to t_0s associated with strong events. In the examples given in this paper, we restrict to one single t_0, enabling a simultaneous optimal focusing of most reflections in the shot gathers; this is sufficient for models with a limited velocity range.

EXAMPLES

First, we consider a situation where the observed wavefield consists of reflected and diffracted waves that interfere in the shot domain. The model (Figure 4) consists of a circular reflector with radius 2600 m located at 1000-m depth, and three embedded point scatterers. The overburden has a constant velocity of 2500 m/s. Fifty-one shot gathers with 128 receivers in each were generated using a Born modeling scheme. Shot and receiver increments are equal to 40 m and 20 m, respectively. Figure 5 shows one of the shot gathers. A strong reflection event masks weak scattered waves. (Note that all plots are displayed in their own dynamic range, without clipping or gain control.) Figure 6 shows the depth image obtained by a Born inversion/migration scheme for the 51 shot gathers. As expected, the scatterers are almost invisible on the image due to their weak amplitude. Only minuscule phase anomalies seem to indicate that the reflector is not completely smooth. For a reliable detection of the scatterers in the seismic image, we would like to construct the image using exclusively diffracted energy from these objects. We do this by applying the sequence of applying the focusing integral 8, muting, applying the defocusing

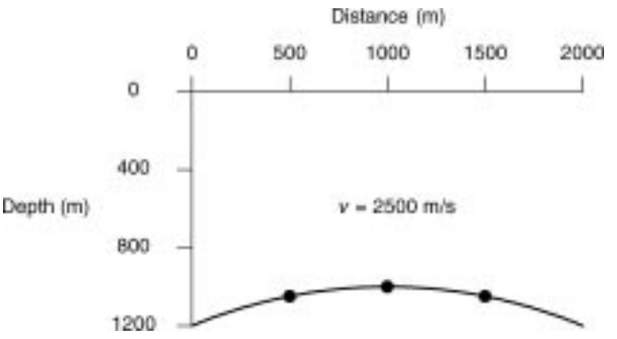

Figure 4. Model with circular reflector (radius 2600 m) located at 1000-m depth, with constant velocity $v = 2500$ m/s. Three point scatterers are located directly on the reflector.

integral 9, and applying expression 4 for one optimal t_0 per shot gather (for example, $t_0 = 1.24$ s gives the best reflection focusing for the shot gather of Figure 5). Figure 7a shows the reflection focus image obtained from the focusing integral 8. The main reflection energy is concentrated in the vicinity of the imaginary source at $\mathbf{x}_{refl} = (1750\text{ m}, 1650\text{ m})$, where $|V^R|$ has a maximum (found by a simple grid search). The energy from the scattering points is smeared out over the reflection focus image and appears in the form of "diffraction smiles." These are much more visible after a muting is applied (Figure 7b, again plotted in its own dynamic range). The reflection focus image is muted by multiplying with a function $\mu(r_0, r_1, r)$, where $r = \|\mathbf{x} - \mathbf{x}_{refl}\|$, $\mu = 0$ for $r < r_0 < r_1$, $\mu = 1$ for $r_0 < r_1 < r$, and smoothly and monotonically increasing from 0 to 1 for $r_0 < r < r_1$, so that r_0 controls the amount of muting and $r_1 - r_0$ controls the transition to unmuted regions. To verify the accuracy of the defocusing operator 9, we first test it on the unmuted reflection focus image. Figure 8 displays the focused-defocused shot gather on top of the original gather (from Figure 5), together with a zoom on the central traces, which shows a very close fit between the two. We then obtain the diffracted shot gathers by applying the defocusing integral 9 to the muted reflection focus image. The result, for the same shot gather, is displayed in Figure 9. Here, the wavefield contains mostly diffracted waves and some residual reflection energy. We repeat the process of focusing-muting-defocusing for all 51 shots.

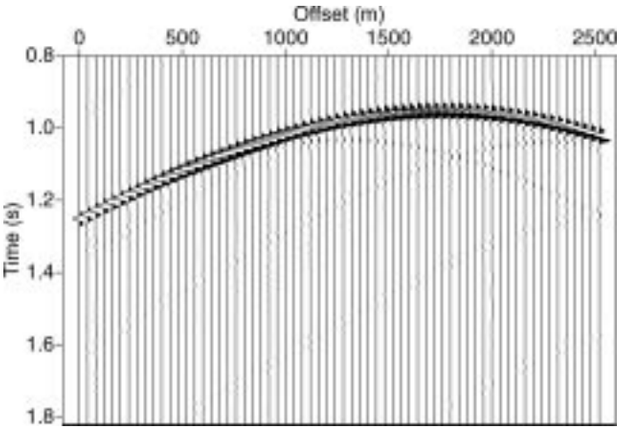

Figure 5. One of the common-shot gathers over the model of Figure 4. A strong reflection event masks weak diffracted waves. Note: all plots are displayed in their own dynamic range without automatic gain control.

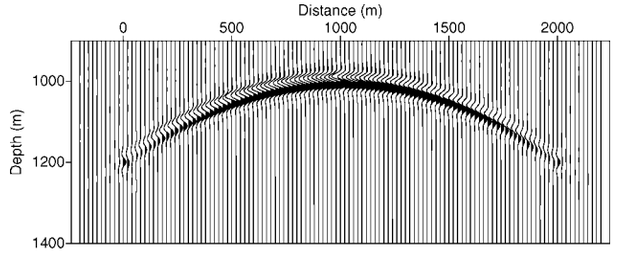

Figure 6. Image obtained by prestack depth migration of full-wave shot gathers. Scatterers are almost invisible due to their weak amplitudes.

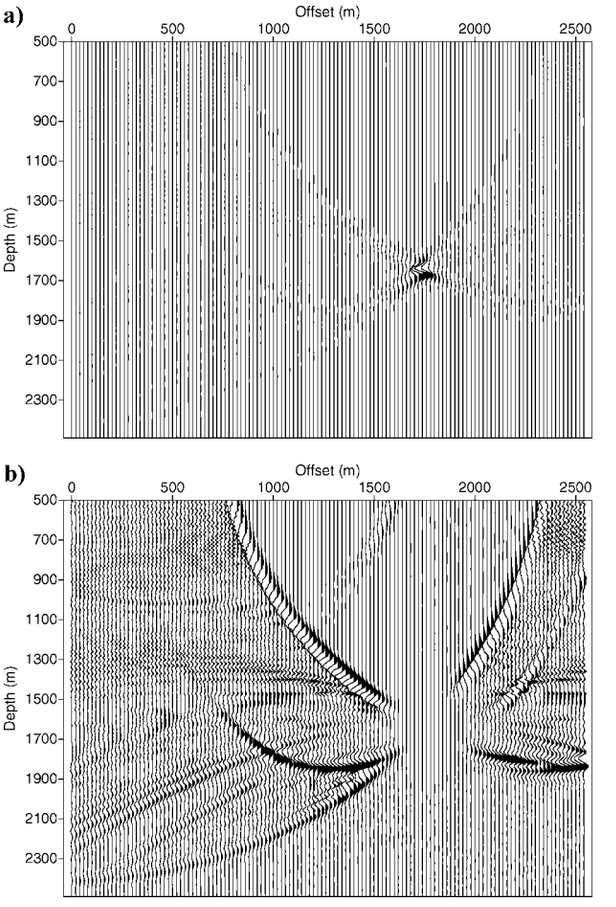

Figure 7. (a) Reflection focus image in pseudodepth domain, corresponding to the shot gather of Figure 5. (b) Muted reflection energy in reflection focus image of (a). Diffraction smiles become visible.

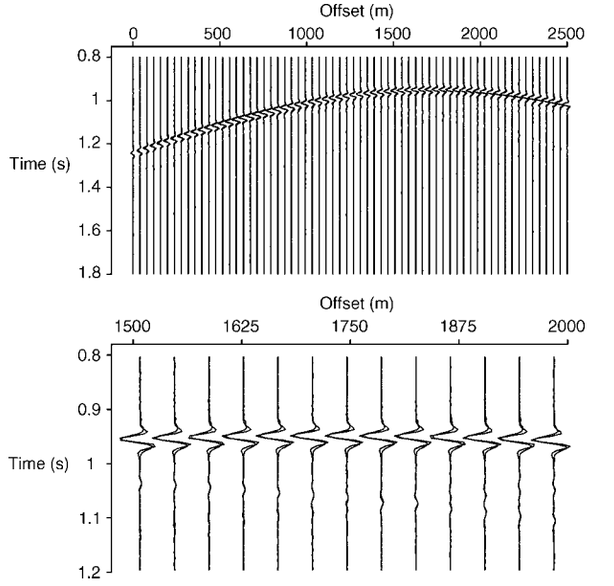

Figure 8. Defocusing test: focused-defocused shot gather (without muting) compared with original gather from Figure 5 (top), plus zoom on central traces (bottom).

The last step of the diffraction imaging procedure consists of migration of all 51 diffracted shot gathers (using the classical diffraction stack 4). Figure 10 shows the result of the migration. It is clear that all three scatterers are well imaged and can be reliably detected from interpreting the image. Two additional diffraction points located at the left and right sides of the figure are caused by edge waves. The reflection interface is attenuated compared to that in the depth image of the original data (Figure 6).

The next example deals with detecting edges in laterally heterogeneous media. Three layers separated by mildly curved faulted interfaces comprise the model shown in Figure 11, with constant velocities equal to 2500, 2700, and 2500 m/s. The faults have a displacement of 20 m. Again 51 shots were generated using a Born modeling scheme, with 128 receivers per shot and a shot and receiver increment of 40 m. Since the wavefield has frequencies up to 60 Hz, the fault displacements are smaller than half the seismic wavelength and, therefore, below the Rayleigh resolution limit. Figure 12 shows one of the shot gathers. As in the previous example, waves diffracted from the fault edges are one or two orders of magnitude weaker than reflected waves from the interfaces. The depth image of the model shown in Figure 13 obtained by prestack Kirchhoff migration with a known velocity model allows interpretation of the strong reflectors (honoring their velocity contrast), but the image at the fault edges is more confused and does not allow reliable localization of the fault edges and their displacement. We attenuated reflections on the shot seismograms by focusing the reflected waves to their imaginary source locations, muting the areas of dominant reflection energy, and calculating the residual wavefield by an inverse focusing operator. One of the resulting seismograms is shown in Figure 14. Diffracted waves from the faults are clearly seen on the seismogram while reflected waves are weakened. We used these diffraction seismograms for depth imaging (by equation 4); the result is shown in Figure 15. All fault edges are clearly imaged and can be easily interpreted (compared to Figure 13). In fact, on close

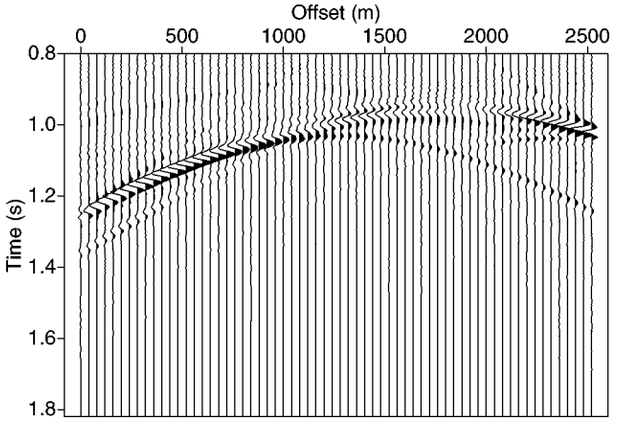

Figure 9. Diffraction shot gather from Figure 5, after focus (Figure 7a), mute (Figure 7b), and defocus.

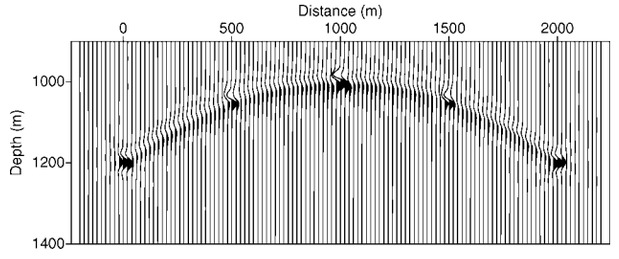

Figure 10. Depth migration of diffraction shot gathers (compare with Figure 6). Three point scatterers are well imaged and can be reliably detected from interpreting the image. Two additional diffractors located at the left and right sides of the figure are caused by the edges of the interface.

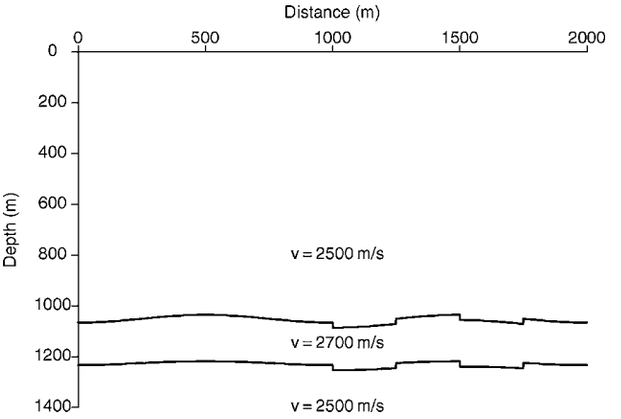

Figure 11. Two-layer model with curved and faulted interfaces. Velocities within the layers are constant and equal to 2500 m/s and 2700 m/s. The fault offset is 20 m.

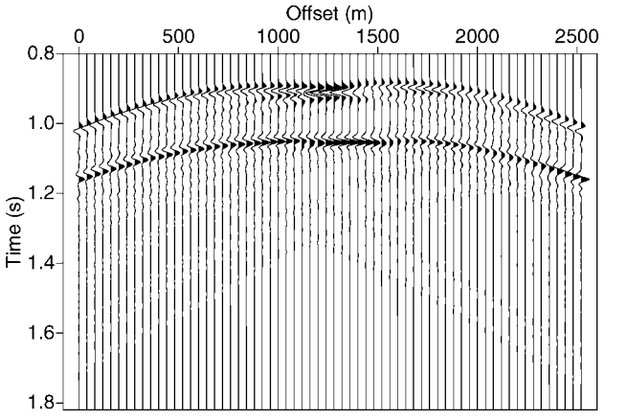

Figure 12. One of the shot gathers over Figure 11.

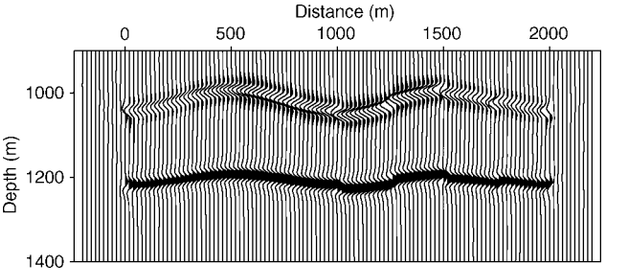

Figure 13. Depth migration of full-wave shot gathers.

inspection (Figure 16) several subwavelength details can be distinguished (if only qualitatively), such as the fault displacement. At each fault edge, we see an X-shaped pattern, where the phase shift with respect to the full-wave image correctly predicts the orientation of the fault and the velocity contrast. As in the previous example, additional diffractors at the left and right sides of the figure are connected to the edges of the model.

Our last example deals with a 2D acoustic data set referred to as Pluto. The 2D model has been designed to replicate the structural and stratigraphic seismic response from a Gulf of Mexico deep-water subsalt prospect (Stoughton et al., 2001). Several variously shaped salt bodies and faulting are incorporated into the model. The seismic data released by the Subsalt Multiples Attenuation and Reduction Technology Joint Venture (SMAART JV) was generated using a finite-difference acoustic waveform modeling scheme. The aim in this study was fault imaging in the shallow part of the model (depth 500–3000 m) above the central salt body. Five main faults can be identified within this model range. Figure 17 illustrates the results of prestack depth migration on the target zone using the correct velocity model. As expected, salt geometry and the fault positions are imaged to their correct positions. Five arrows indicate the termination of reflectors on four different fault planes. However, due to illumination effects, the fault planes themselves are hardly distinguishable; in fact, the only evidence they leave are the jumps in the reflectors. We applied our diffraction imaging scheme to the shot seismograms. Figure 18 shows one of the common-shot gathers for the full wavefield. First, we focused reflections to their imaginary source positions and attenuated them by muting the areas of energy concentration. Figure 19a shows the reflection focus image of Figure 18,

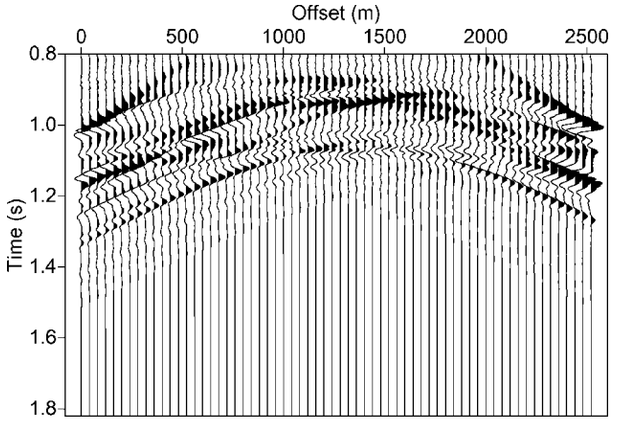

Figure 14. Shot gather of Figure 12 with reflections suppressed.

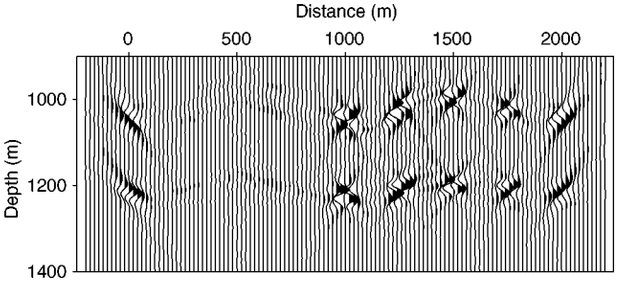

Figure 15. Depth migration of diffraction shot gathers. Fault positions as well as reflector edges are clearly visible (and easy to interpret) compared to Figure 13.

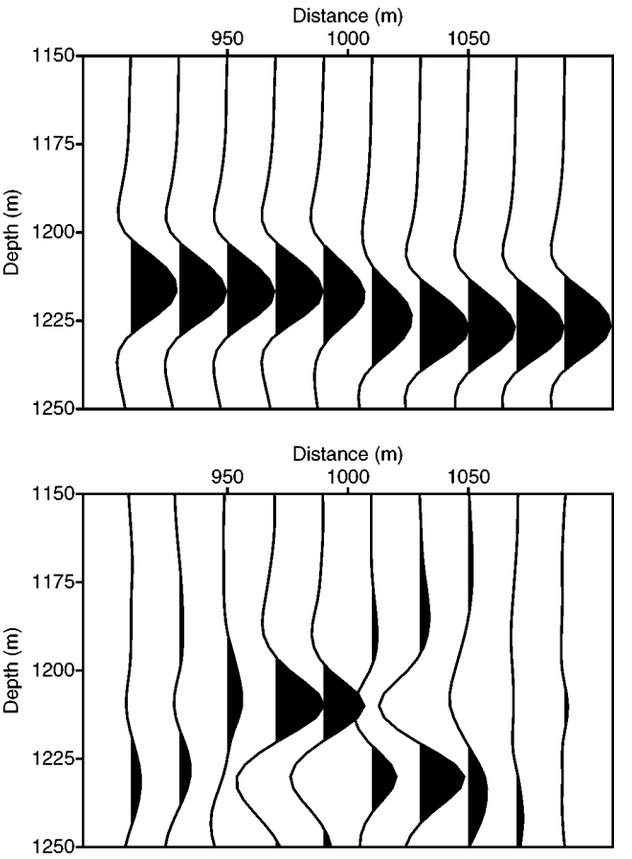

Figure 16. Zoom on full-wave image (top, zoom from Figure 13) and diffraction image (bottom, zoom from Figure 15) at (1000 m, 1200 m). The diffraction image allows for a much better and less ambiguous interpretation of the fault geometry than the full-wave image.

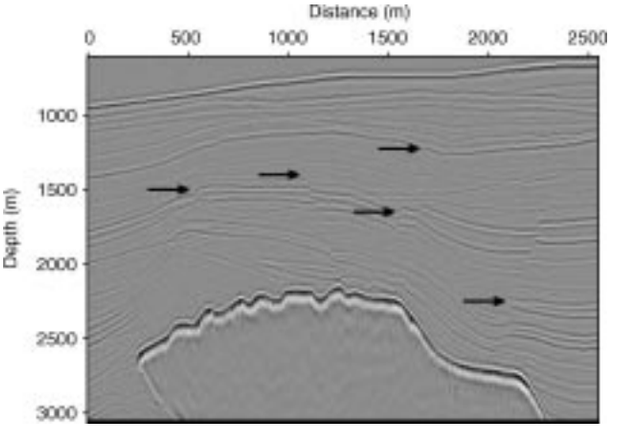

Figure 17. Depth migrated image from Pluto data set. Fault planes (shown by arrows) are hard to distinguish.

Figure 19b the muted version. The defocusing operator then constructed the residual wavefield, containing mostly diffractions. The resulting residual seismogram is shown in Figure 20. Figure 21 shows the results of depth migration applied to the residual common-shot seismograms (again using the classical diffraction stack 4). All five fault planes shown by arrows in the figure are clearly imaged and can be easily interpreted. Strongly curved elements of the salt body are also well defined in the image. Due to the discrimination on moveout, a consistent multiple in the image of Figure 17 (extending from depth 2000 m at the left to about 1500 m at the right) is inadvertently suppressed in Figure 21. It is also interesting to note that numerous diffraction patterns along the smoothed interfaces appear. These are certainly caused by the grid representation used in the finite-difference data modeling and strong diffracted wavefield created by the modeling scheme. The ability to detect these artificial numerical scatterers illustrates once more the potential of the focusing-defocusing approach to diffraction imaging.

DISCUSSION AND CONCLUSIONS

Diffractions offer a different perspective on seismic image resolution and the way it is achieved. Traditional processing/migration regards the diffractive wavefield component as noise and ignores the structural information it conveys; in fact, one can argue that migration does not even need real diffractions to produce images of the same quality. First, during processing (NMO/DMO, multiple attenuation, velocity estimation, stacking), events not originating from a smooth and strong reflector are usually filtered out. Second, conventional migration algorithms are designed in a way which emphasizes specular reflections. Kirchhoff migration kernels are usually derived based on a high-frequency or stationary-phase approximation. Even the classical isotropic diffraction stack favors constructive

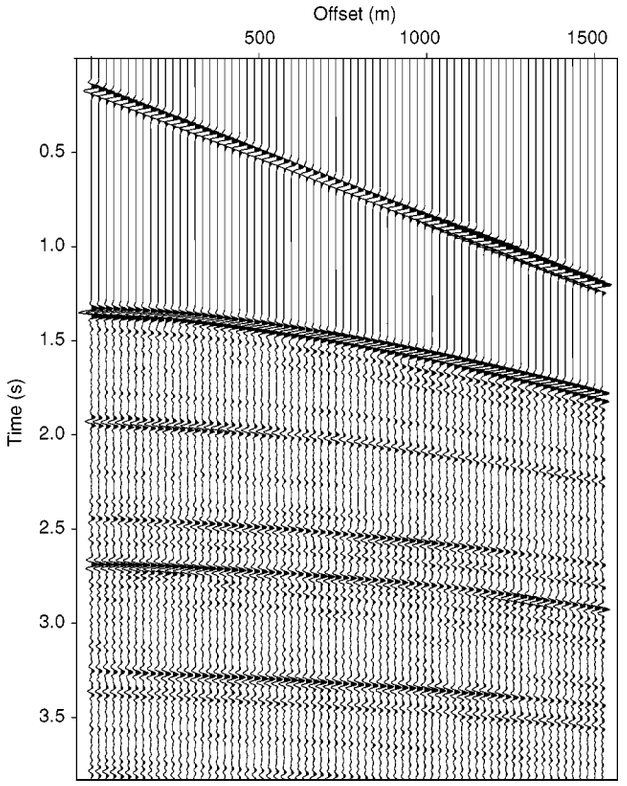

Figure 18. One of the full-wave shot gathers.

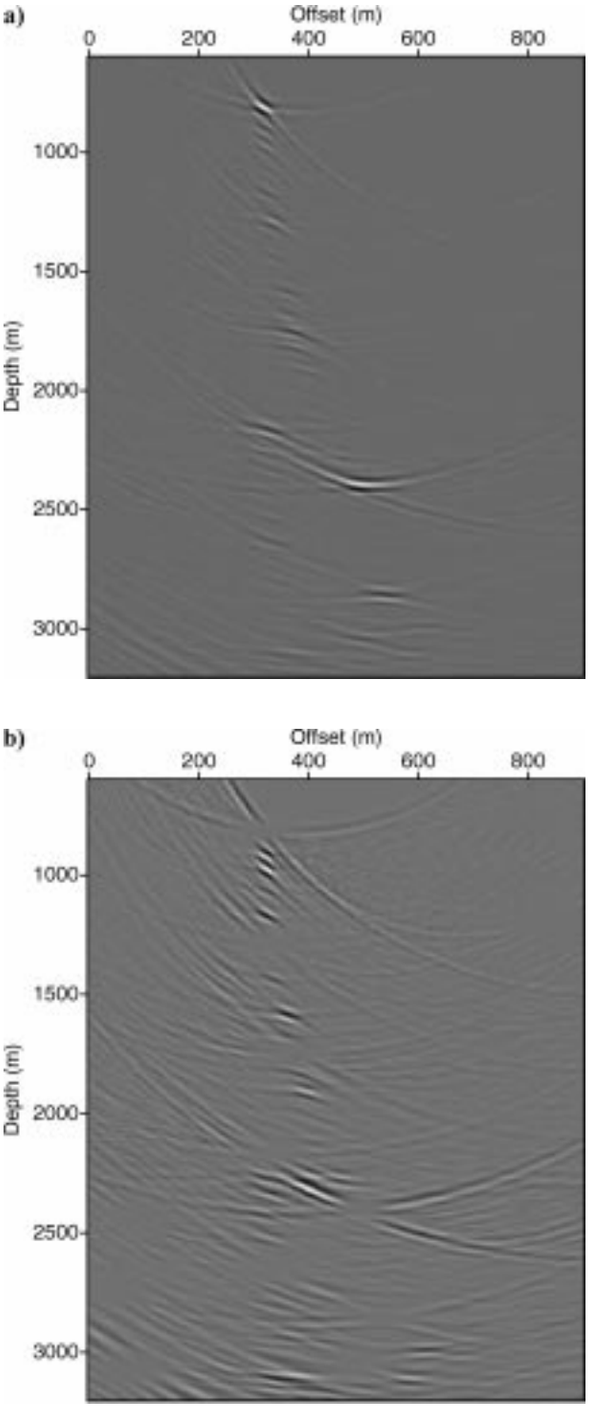

Figure 19. (a) Reflection focus image from Figure 18 in pseudodepth domain. Several focuses from different reflection events are visible. (b) Mute of reflection focus image of (a). Diffraction energy remains.

interference of reflections to isolated scatterings. The result is that images tend to highlight reflectors and obscure nonreflecting structures, such as small faults, edges, pinch-outs, and small scattering objects. It is precisely this detailed structural information that is the main objective of seismic interpretation. To improve the resolution and enhance details of the size of the seismic wavelength, several techniques have been proposed and are being applied in the industry. These techniques are image oriented, in the sense that they operate on the image after processing and migration. They are successful, to a certain degree, in revealing details that are masked in the seismic image. However, if no discrimination is made between the different types of waves involved in the imaging, the resolution is essentially limited by the Rayleigh criterion. Any detail smaller than half the seismic wavelength cannot be interpreted in an objective, unambiguous way. Apart from the resolution limit, the image-oriented techniques do not distinguish between real structural details and false edges created by processing artifacts or an incorrect migration velocity. In such situations, they accomplish little more than image cosmetics. As a result, in some geophysical applications, the value of the seismic image is unfairly depreciated in favor of other sources of information (well data or geological evidence). We take a few steps back in the processing/migration sequence and advocate a data-driven approach to image resolution, using diffractions. Diffractions are reliable indicators of small structural characteristics, and distinguish between real diffracting edges and migration artifacts (quality checked by common-image gathers). Also, under idealized circumstances (such as a low noise level), they allow recovery of subwavelength details. This makes diffractions the key to seismic superresolution.

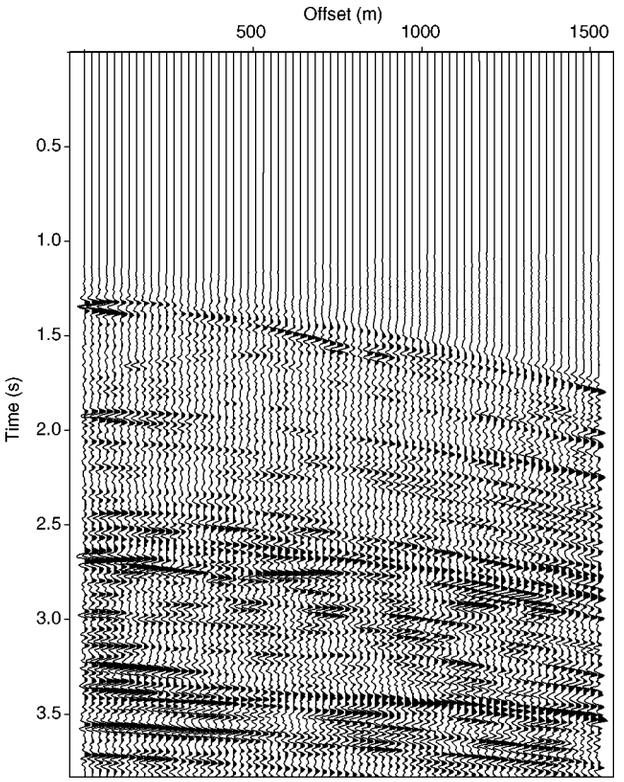

Figure 20. Diffraction shot gather from defocusing the muted reflection focus image of Figure 19b. The wavefield contains mostly scattered waves (compare with Figure 18).

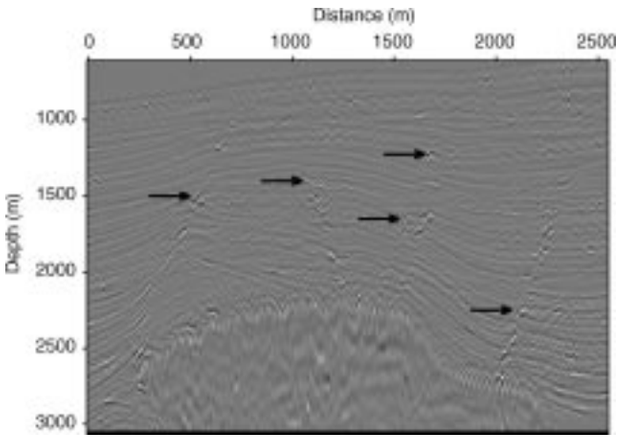

Figure 21. Depth migration of diffraction shot gathers. All fault planes (shown by arrows) are clearly imaged and can be easily interpreted. Note the existence of numerous grid diffraction patterns on top of the salt body, which are detected by the focusing-defocusing algorithm.

Due to their geometrical properties, diffractions are best studied and analyzed in the prestack domain and before migration. The main challenges of diffraction analysis are that diffractions are usually tangent to reflections, and that they are typically one or two orders of magnitude weaker. To separate them from the full wavefield, we propose to exploit different moveout properties and focus reflections to their own imaginary source points. We do this by constructing the (hypothetical) reflection traveltime curve for each event crossing zero offset in the shot gathers and stacking the energy along it. The resulting reflection focus image in a pseudodepth domain contains sharply focused reflection points, with diffraction energy smeared out over large areas. We mute the reflection energy and apply a defocusing integral to construct the diffracted shot gather. The classical diffraction stack is then applied to the diffraction shot gathers.

We note here that, once the reflection focus image has been established, muting-defocusing is not the only option to obtain the diffraction shot gather. An alternative is to find the reflection focus point, apply a median filter along the associated reflection traveltime curve in the shot gather, and subtract the filtrate from the full wavefield. The situation is very similar to standard τ-p multiple attenuation, and both options have their own advantages (Landa et al., 1999b). When the reflection and diffraction events strongly interfere in the time domain, but separate well in the pseudodepth domain, filtering and subtraction will damage the signal. On the other hand, defocusing usually suffers from weak linear artifacts (visible in Figure 9). Which alternative is best in a given situation is still a topic of ongoing research.

We emphasize that the crux of the reflection focusing is that it is not important *where* the reflection focuses, but only *that* it focuses. Another point to keep in mind is that there is no sharp distinction between reflections and diffractions, so that there is no complete removal of reflection events, only attenuation. Our proposed focusing-muting-defocusing approach can be implemented both in a macrovelocity dependent and

independent context. In situations where an accurate velocity model is available (such as in the framework of prestack depth migration), the reflection traveltime curve can be found by ray tracing. Depending on the accuracy of the velocity model, or its focusing capacity, it will focus reflections to points or to sharp localized caustics. A proper setting of the muting parameters ensures that the reflection attenuation is sufficient for the subsequent diffraction imaging. Accurate velocity knowledge is not available in many cases, so we concentrate in this paper on the macromodel independent context. Lack of velocity information has two implications: an extra focusing parameter is needed in the form of the zero-offset time t_0, and an assumption on the reflection traveltime curve is needed. Here, we use the homeomorphic imaging principle, which takes the reflected wavefronts as spherical and their associated traveltime curves as hyperbolic. Depending on the hyperbolicity, the reflection energy will again focus to one point, or rather to a sharp localized caustic, again to be handled by a proper setting of muting parameters. In the model-independent context, we typically need to focus and attenuate each major reflection event crossing zero offset separately. In models with a limited velocity range, as presented in this paper, this can be simplified to one single t_0, enabling optimal focusing of all reflections events simultaneously. Our implementation can be generalized to 3D and different acquisition geometries without further theoretical complications: similar types of focusing and defocusing integrals can be set up, the search for maximum reflection focus becomes a 3D search, and the muting function has to be extended. While we do not address the CPU issue in detail in this paper, the cost of our diffraction imaging may be estimated to be of the order of three times the prestack depth imaging [consisting of (1) focusing the shot gathers, (2) defocusing the muted reflection focus images, and (3) imaging the diffraction shot gathers; the grid search is relatively cheap compared to these steps], which we think is an acceptable price for the increased resolution and reliable interpretability of diffraction images.

There is a great potential for research and development in diffraction imaging, and many issues are still to be investigated. First of all, the relation to resolution and superresolution needs to be further explored. In the current paper, we considered only kinematic properties; the technique may be modified to include true-amplitude modeling, so that a measure of diffractivity becomes available next to the traditional reflectivity. Also, we do not make here a distinction between scattered waves from small objects and edge diffractions; however, their different dynamical behavior can be analyzed and exploited in more refined algorithms. The phase content of the diffraction image can be analyzed to extract more information on fault edges, their orientation, and their relation to reflectors. In three dimensions, diffractions differentiate between edges and tips (Klem-Musatov, 1994). In 4D (time-lapse) studies, diffractions can help to monitor the displacement of the oil/gas–water contact during production.

In any case, we have shown that diffraction imaging is feasible, and that it produces reliable images with detail unachievable by conventional means. We strongly believe that such images should be made available to the interpreter as a standard supplement to full-wave seismic images.

Diffractions have been the stepchildren of traditional processing/imaging. However, if they receive the attention they deserve, we will be able to see the invisible.

ACKNOWLEDGMENTS

We are grateful to the reviewers for fair and constructive criticism. T. J. M. thanks Fugro-Jason for approval to participate in the paper.

REFERENCES

Berryhill, J. R., 1977, Diffraction response for nonzero separation of source and receiver: Geophysics, **42**, 1158–1176.
Bertero, M., P. Boccacci, and M. Piana, 1997, Resolution and superresolution in inverse diffraction, *in* G. Chavent and P. C. Sabatier, editors, Inverse problems of wave propagation and diffraction: Springer, 1–17.
Beylkin, G., 1985, Imaging of discontinuities in the inverse scattering problem by inversion of a causal generalized Radon transform: Journal of Mathematical Physics, **26**, 99–108.
Born, M., and E. Wolf, 1959, Principles of optics: Pergamon Press.
Červený, V., 2001, Seismic ray theory: Cambridge University Press.
Chen, J., and G. T. Schuster, 1999, Resolution limits of migrated images: Geophysics, **64**, 1046–1053.
de Bazelaire, E., 1988, Normal moveout revisited: inhomogeneous media and curved interfaces: Geophysics, **53**, 143–157.
Docherty, P., 1991, A brief comparison of some Kirchhoff integral formulas for migration and inversion: Geophysics, **56**, 1164–1169.
Fehmers, G. C., and C. Höckers, 2003, Fast structural interpretation with structure-oriented filtering: Geophysics, **68**, 1286–1293.
Gerchberg, R. W., 1974, Super-resolution through error energy reduction: Optica Acta, **21**, 709–720.
Gersztenkorn, A., and K. J. Marfurt, 1999, Eigenstructure-based coherence computations as an aid to 3-D structural and stratigraphic mapping: Geophysics, **64**, 1468–1479.
Goldin, S., V. Khaidukov, V. Kostin, S. Ryan, and V. Tcheverda, 2000, Separation of reflected and diffracted objects by means of Gaussian beams decomposition, *in* A. Bermudez, D. Gomez, C. Hazard, P. Joly, and J. Roberts, editors, Proceedings of 5th International Conference on Mathematical and Numerical Aspects of Wave Propagation: Society for Industrial and Applied Mathematics and Institute de Recherche en Informatique et en Automatique.
Hagedoorn, J. G., 1954, A process of seismic reflection interpretation: Geophysical Prospecting, **2**, 85–127.
Hubral, P., J. Schleicher, and M. Tygel, 1996, A unified approach to 3-D seismic reflection imaging, Part I: Basic concepts: Geophysics, **61**, 742–758.
Hu, J., G. T. Schuster, and P. A. Valasek, 2001, Poststack migration deconvolution: Geophysics, **66**, 939–952.
Kanasewich, E. R., and S. M. Phadke, 1988, Imaging discontinuities on seismic sections: Geophysics, **53**, 334–345.
Keller, J. B., 1962, Geometrical theory of diffractions: Journal of the Optical Society of America, **52**, 116–130.
Keydar, S., B. Gelchinsky, and A. Berkovitch, 1996, Common shot point stacking and imaging method: Journal of Seismic Exploration, **5**, 261–274.
Klem-Musatov, K., 1994, Theory of seismic diffractions, edited by F. Hron, and L. Lines: SEG.
Krey, T., 1952, The significance of diffraction in the investigation of faults: Geophysics, **17**, 843–858.
Landa, E., I. Belfer, and S. Keydar, 1999b, Multiple attenuation in the parabolic τ-p domain using wavefront characteristics of multiple generating primaries: Geophysics, **64**, 1806–1815.
Landa, E., B. Gurevich, S. Keydar, and P. Trachtman, 1999a, Application of multifocusing method for subsurface imaging: Journal of Applied Geophysics, **42**, 283–300.
Landa, E., and S. Keydar, 1998, Seismic monitoring of diffraction images for detection of local heterogeneities: Geophysics, **63**, 1093–1100.
Landa, E., V. Shtivelman, and B. Gelchinsky, 1987, A method for detection of diffracted waves on common-offset sections: Geophysical Prospecting, **35**, 359–374.
Levin, S. A., 1998, Resolution in seismic imaging: Is it all a matter of perspective?: Geophysics, **63**, 743–749.
Moser, T. J., S. A. Petersen, and E. Landa, 2000, Diffractivity analysis of VSP data: 70th Annual International Meeting, SEG, Expanded Abstracts, 758–761.
Neidell, N. S., 1997, Perceptions in seismic imaging, Part 2: Reflective and diffractive contributions to seismic imaging: The Leading Edge, **16**, 1121–1123.
Nemeth, T., S. Hongchuan, and G. Schuster, 2000, Separation of signal and coherent noise by migration filtering: Geophysics, **65**, 574–583.

Papziner, U., and K. P. Nick, 1998, Automatic detection of hyperbolas in georadargrams by slant-stack processing and migration: First Break, **16**, 219–223.
Santos, L., J. Schleicher, M. Tygel, and P. Hubral, 2000, Seismic modeling by demigration: Geophysics, **65**, 1281–1289.
Stoughton, D., J. Stefani, and S. Michell, 2001, 2D elastic model for wavefield investigations of subsalt objectives, deep water Gulf of Mexico: 63rd Annual Meeting, European Association of Geoscientists and Engineers, session A-33.
Timoshin, Y. V., 1978, Seismic pulse holography (in Russian): Nedra.
Trorey, A. W., 1970, A simple theory for seismic diffractions: Geophysics, **35**, 762–784.
Tygel, M., J. Schleicher, and P. Hubral, 1996, A unified approach to 3-D seismic reflection imaging, Part II: Theory: Geophysics, **61**, 759–775.
Zavalishin, B. R., 1982, Diffractions over deposit edges: Stanford Exploration Project Report **32**, 125–136.
——— 2000, Diffraction problems of 3D seismic imaging: Geophysical Prospecting, **48**, 631–645.